

412TW-PA-14145



NUMERICAL PREDICTIONS OF STATIC-PRESSURE-ERROR CORRECTIONS FOR A MODIFIED T-38C AIRCRAFT

4
1
2
T
W

Daniel A. Reasor Jr.
Keerti K. Bhamidipati
Reagan K. Woolf

AIR FORCE TEST CENTER
EDWARDS AFB, CA

December 2014

Approved for public release ; distribution is unlimited.
412TW-PA-14145

AIR FORCE TEST CENTER
EDWARDS AIR FORCE BASE, CALIFORNIA
AIR FORCE MATERIEL COMMAND
UNITED STATES AIR FORCE

Numerical Predictions of Static-Pressure-Error Corrections for a Modified T-38C Aircraft

Daniel A. Reasor, Jr., * Keerti K. Bhamidipati, * and Reagan K. Woolf[†]
U.S. Air Force, Edwards Air Force Base, California 93524

DOI: 10.2514/1.C032925

The objective of this work was to highlight modeling considerations for estimating the required static-pressure-error corrections using computational fluid dynamics. This work was performed to complement the U.S. Air Force Test Pilot School activities that used a T-38C aircraft with a previously untested Pitot-static system. Before the flight test, it is highly desirable to have an estimate of how any modifications will affect sensor performance, and to possess the capability to explain any discrepancies from previous test programs. Estimates of this kind are only obtainable via wind-tunnel tests or through modeling and simulation. This work presents the computational fluid dynamics requirements and methodologies needed to estimate the static-pressure-error correction of a T-38C in the subsonic, transonic, and low supersonic regimes. Estimates are validated with flight-test results, and proposed solutions for further reduction of static-pressure error via modifications to the flight-tested Pitot-static-probe geometry are included.

Nomenclature

D	= test-boom diameter, in.
d	= probe diameter, in.
M	= Mach number
p	= pressure, psi
q	= dynamic pressure, psi
x	= distance from the Pitot-static-probe tip, in.
α	= angle of attack, deg
β	= angle of sideslip, deg
Δp	= $(p_{\text{measured}} - p_{\infty})$, pressure error, psi
Δs	= grid-spacing or element-edge length, in.
ρ	= density, slugs/in. ³ (slug · ft/in. ⁴)

Subscripts

c	= compressible
pc	= pressure correction
sic	= static indicated corrected
∞	= freestream
\perp	= wall normal

I. Introduction

THE fleet of T-38C aircraft at the U.S. Air Force (USAF) Test Pilot School (TPS) is used to train the next generation of flight-test pilots, navigators, and engineers. Because of the unique nature of the curriculum requirements of the TPS, these aircraft use instrumentation equipment that exceed production T-38C capabilities, including the ability to accurately measure yaw, angle of attack, and Pitot-static (YAPS) data. These YAPS systems are mounted on test nosebooms that extend several feet forward of the aircraft nose. To accurately measure airspeed, altitude, and Mach number, the Pitot-static element of the YAPS must not be influenced significantly by the pressure field generated by itself, the noseboom, or the nose of the aircraft; otherwise, it must be corrected using an air-data

Received 1 April 2014; revision received 7 August 2014; accepted for publication 3 September 2014; published online 15 December 2014. This material is declared a work of the U.S. Government and is not subject to copyright protection in the United States. Copies of this paper may be made for personal or internal use, on condition that the copier pay the \$10.00 per-copy fee to the Copyright Clearance Center, Inc., 222 Rosewood Drive, Danvers, MA 01923; include the code 1542-3868/14 and \$10.00 in correspondence with the CCC.

*Testing Techniques Flight, 412th Test Wing, 812th Test Support Squadron. Member AIAA.

[†]Technical Expert, Performance and Flying Qualities Flight, 412th Test Wing, 773rd Test Squadron. Senior Member AIAA.

computer to meet the TPS, military specification (MIL-SPEC) [1], and Federal Aviation Administration (FAA) airspace regulations [2].

Designers used computational fluid dynamics (CFD) simulation results [3] to estimate the recommended extension length for the test noseboom to be installed in the test fleet. Simulations were used to predict the distribution of static-pressure and angle-of-attack errors in front of the production Pitot-static probe up to distances of 8 ft, and aimed to capture the extent and magnitude that the aircraft nose cone, fuselage, and canopy influence the flowfield in front of the aircraft.

Flight tests of the test noseboom installed on the T-38C revealed discrepancies between predicted and measured static-pressure errors. Subsequent investigations determined that estimating accurate static-pressure errors using CFD requires accurately modeling test-noseboom geometries to capture local influences on the pressure field. This paper focuses on the design of special flight-test hardware, but the results are applicable to the design of production Pitot-static sensor installations on manned and unmanned, civil, and military air vehicles.

II. Background

Static pressure is typically measured in two ways during flight: with a Pitot-static probe or via a flush-mounted port on the fuselage; typically, fighter aircraft employ the former, and cargo aircraft employ the latter. The distribution of the static pressure on the aircraft wetted surface is influenced by several factors, including angles of attack α and sideslip β , Mach number, dynamic pressure q , and aircraft configuration. Furthermore, choosing a location for a static-pressure port that is resilient to changes in flight conditions can be a challenge. The difference between the measured and true static pressures, $\Delta p = p_{\text{measured}} - p_{\infty}$, normalized by compressible dynamic pressure, $q_c = p_{\text{total}} - p_{\infty}$, is commonly referred to as the static-pressure error ($\Delta p/q_c$). At high α or large β conditions, the static-pressure error can be exacerbated by flow entering the static ports on the windward side of the probe, while leeward-side ports are subjected to above ambient pressure if the flow is separated. Errors of this type cannot be avoided for all flight conditions, but instrumentation designers can use knowledge of the pressure distribution to place static-pressure ports at locations that are more resilient. A static-pressure error manifests itself as errors in indicated airspeed, altitude, and Mach number to the pilot. Acceptable error magnitudes are prescribed by flight-test accuracy requirements, MIL-SPECs [1], or FAA regulations [2]. As a result, air-data measurements must be either corrected to values and variation within the provided standard by employing an air-data computer or with specialized instrumentation.

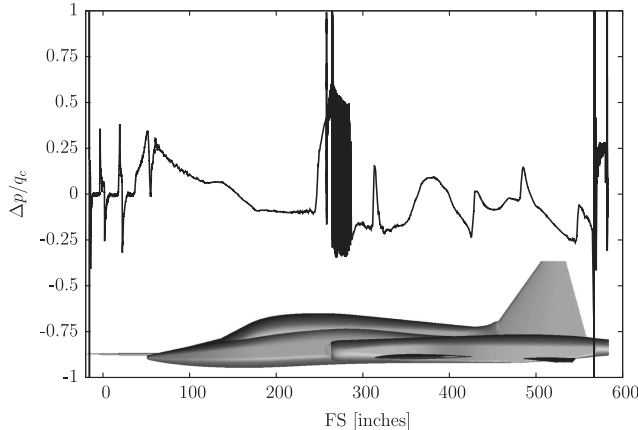


Fig. 1 CFD simulated static-pressure-error ($\Delta p/q_c$) distribution on a T-38C plotted against fuselage-station (FS) location at the waterline corresponding to the noseboom centerline.

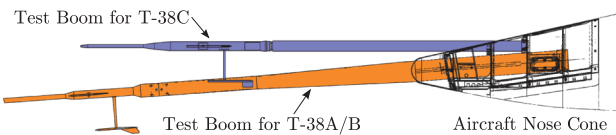


Fig. 2 Illustration of the test noseboom and YAPS geometries on the T-38A/B models and that used on the T-38C.

The surface distribution of the static-pressure error ($\Delta p/q_c$) can be used to reveal local variations due to major elements of the aircraft and control surfaces, specific weapons configurations, as well as instrumentation and antenna (see Fig. 1). Ideal locations for pressure ports, total-air-temperature sensors, etc., can then be determined. Peaks, either positive or negative, in the static-pressure-error distribution are usually attributed to major components, but standing or oscillating shock waves at transonic conditions can also be a source. Unfortunately, the distribution is rarely available to an instrumentation engineer posed with the task of determining what sensor package is best suited for a particular test program, and that is a primary reason why corrections are employed.

For most test configurations, it is advantageous to use a longer noseboom to place the Pitot-static probe in the region fore of the aircraft nose cone where static-pressure errors are less susceptible to aircraft influences. However, structural limitations often prevent the noseboom length from reaching the region of zero static-pressure error. Although it is not consistent with the requirements of a production fighter aircraft (especially from an observability standpoint), longer nosebooms are commonly used in the test environment to obtain static- and dynamic-pressure data that are independent of aircraft configuration. Test aircraft with these unique instrumentation packages are typically limited in number, but they serve as a truth source for the development and calibration of production systems used by a much larger fleet of aircraft.

Trends found in historical literature [4–7] regarding influences on static-pressure error for noseboom-mounted probes should be consulted before selecting a noseboom and probe design. These trends highlight the poor transonic performance of near-body installations. To reduce error, static-pressure ports are placed as far fore of the aircraft as possible. Similarly, increasing the distance from a ramp on the noseboom to the static-port location can reduce error for a range of Mach numbers. However, static ports installed too near to the tip of the probe can be affected by spillage effects in the vicinity of the total pressure port. For the noseboom-mounted Pitot-static probes, the static-pressure error increases with increasing Mach number in the transonic regime; this is primarily due to strong pressure waves propagating forward from the aircraft nose, but also due to the smaller amplitude waves propagating from changes in

geometry on the noseboom/probe system itself. Once the aircraft reaches the supersonic regime, the static-pressure error will be at a minimum because the aircraft bow shock is downstream of the static-pressure orifices, and pressure waves do not propagate forward in that regime.

Errors induced by nonzero α and β are typically addressed with the use of multiple static-pressure ports. A boom with two ports on the bottom surface is generally resilient to changes in α for ranges from -10 to 15 deg in the subsonic and supersonic regimes, but the exact α range can depend on the circumferential locations [4]. A greater number of ports are often used for aircraft capable of α as high as 25 deg, but pressure fluctuations are difficult to mitigate for α greater than 35 deg.

Because of the presence of the static-port orifice, streamlines are deflected into the cavity generating a system of eddies termed *cavity vortices*. Under these conditions, the pressure will be slightly higher than the true value at the surface because the velocity is not zero relative to the wall. Generally, a large depth-to-diameter ratio is desired to ensure that the flow within the cavity is fully developed, but is usually limited by probe size, internal plumbing, and tip-heater circuitry. The static-pressure error increases with increasing static-port-orifice diameter and orifice Reynolds number, whereas it decreases with increasing port depth [8].

To meet the demand for accurate static-pressure and altitude readings in flight, aerodynamically compensated probes were developed [9]. Curving the probe surface aft of the static port to generate a favorable pressure gradient and offset the static-pressure error is one very effective compensating technique. Designing these probes requires the calculation or previous knowledge of the static-pressure field on the probe surface for a range of flight conditions. The type of compensation used may vary (e.g., forward vs backward), depending on how the aircraft influences the pressure field in the vicinity of the instrumentation. Typically, the presence of the aircraft will generate a higher than ambient pressure upstream of the nose cone where probes are commonly mounted. The modeling and simulation activities of Luo and Bao [10] used the transonic small transverse perturbation equation to predict error compensation, but the more modern work of Latif et al. [11] demonstrated that compensated Pitot-static probes can be simulated accurately for subsonic and transonic flows by validating two-dimensional Reynolds-averaged Navier–Stokes (RANS) computations with wind-tunnel experiments for subsonic and supersonic conditions.

III. Flight-Test Description

Legacy flight-test nosebooms that were installed on the T-38A/B models are incompatible with the newer T-38C aircraft due to differences in aircraft configuration. As a result, a newly designed test noseboom and YAPS system was needed. Figure 2 illustrates the differences between the test noseboom used on the T-38A/B and the

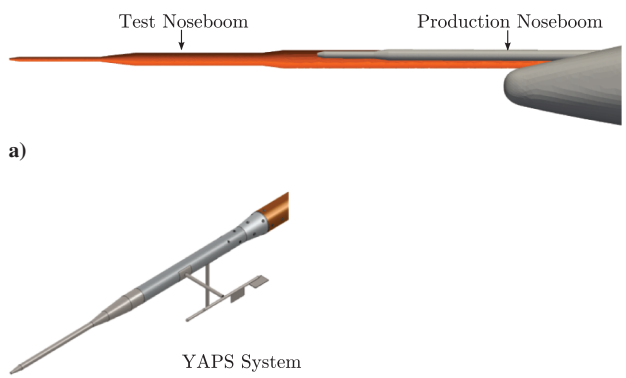


Fig. 3 Geometric descriptions of the YAPS system and nosebooms: a) a profile comparison between test and production T-38C noseboom geometries, and b) illustration of the YAPS system.

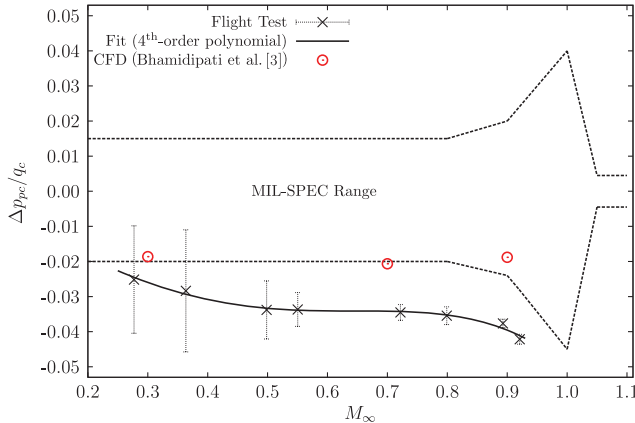
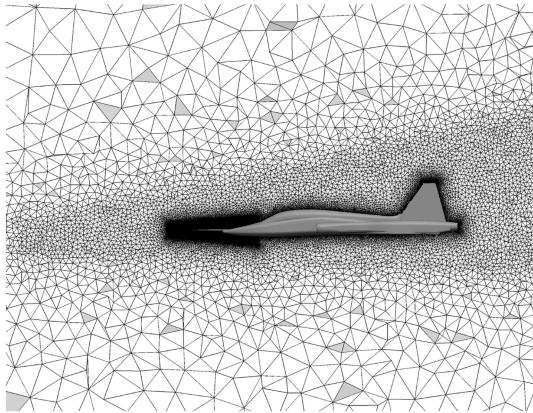
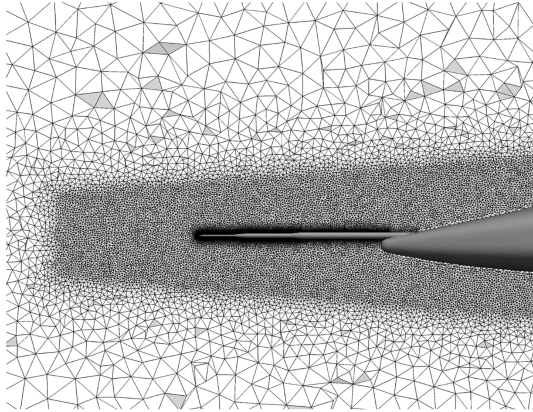


Fig. 4 Comparison between flight-test data from formation flights and CFD-predicted static-source-error corrections; the fourth-order polynomial fit is typical of that used by air-data computers to correct for the static source error.



a) Full aircraft



b) Noseboom

Fig. 5 T-38C full-aircraft-grid views.

T-38C models. Because of the expense and lead times associated with wind-tunnel tests, it is not feasible to perform experiments for every nonproduction test program in the current fiscal climate. Thus,

modeling and simulation are playing a more prevalent role in flight-test activities through the use of CFD.

The modified test noseboom of the T-38C, which is longer than the production boom (see Fig. 3a), also employs a YAPS system (Fig. 3b) to measure precise air data in support of TPS curriculum sorties. The objective of this modification was to obtain quality air data that supported the TPS curriculum objectives while preserving sufficient accuracy to allow the aircraft to fly cross-country missions in the national airspace. Calibration flight tests were completed by the USAF TPS, and postflight analysis was performed by the 773rd Test Squadron.

Following the modification of the T-38C aircraft with a test noseboom, calibration flight tests were conducted to determine the static-pressure errors. Three calibration-flight-test techniques [7] were employed: 1) flight in formation with an unmodified T-38C aircraft, whose production-representative noseboom and air-data computer with calibrated static-pressure-error-correction curves provided truth source data; 2) tower flybys, in which the instrumented flyby tower and theodolite provided truth source data; and 3) level accelerations and decelerations through transonic Mach numbers, in which GPS altitude tracking and rawinsonde weather balloons provided truth source data.

A postflight analysis [12] revealed that the test noseboom/YAPS system incurred static source errors in excess of what was originally estimated from CFD simulations in Bhamidipati et al. [3] by extracting the static-pressure error in front of the production probe. The discrepancy between the flight-test data from formation flights and the CFD predictions is illustrated in Fig. 4. The flight test uncertainties shown in Fig. 4 include estimated error components for the unmodified T-38C chase aircraft air data computer (truth source), formation flight errors, and modified T-38C air data computer errors. The magnitudes of the uncertainties were inversely related to Mach number because the static source error corrections have an indicated-corrected q_c in the denominator. The large static-pressure errors limited the aircraft to flying at inefficient Mach numbers when outside of restricted military airspace due to federal airspace regulations [2,13]. Further CFD simulation studies were conducted to investigate the differences between preflight static-pressure-error estimates and flight-test results, and to evaluate methods for reducing the magnitude of the errors to acceptable levels.

IV. CFD Methodology and Setup

The modeling and simulation efforts presented in this work make use of the unstructured node-centered finite-volume-based [14–17] compressible flow solver AERO-F, which is a major module of the multiphysics AERO Suite of Codes by CMSSoft, Inc. [18] employed in related USAF aeroelastic-simulation research [19–22]. The outer mold line of the standard T-38C aircraft is modified with the test-boom geometry based on measurements of the test T-38C aircraft.

The fluid is modeled as air governed by the ideal-gas equation of state with constant specific-heat ratio and Sutherland's viscosity law for viscous computations. The steady-state compressible Euler equations were solved for inviscid computations, and the steady-state compressible RANS equations with the one-equation Spalart–Allmaras [23] turbulence model were used for viscous computations. The slip boundary condition was enforced on the aircraft surface for the inviscid Euler simulations. The no-slip condition was enforced only on the noseboom and probe surfaces for the viscous computations to mitigate the expense of boundary-layer grid

Table 1 Computational-grid details for the four-level refinement study

	Grid points	Elements	Spatial resolution ^a (Δs)	Wall-normal spacing ^a (Δs_{\perp})
Coarse (Euler)	2.45×10^6	14.4×10^6	1.5×10^{-1}	1.5×10^{-1}
Medium (Euler)	2.49×10^6	14.6×10^6	1.0×10^{-1}	1.0×10^{-1}
Fine (Euler)	2.61×10^6	15.4×10^6	5.0×10^{-2}	5.0×10^{-2}
Very fine (Euler)	3.53×10^6	20.7×10^6	4.0×10^{-2}	4.0×10^{-2}
Very fine (RANS)	7.58×10^6	27.6×10^6	4.0×10^{-2}	1.0×10^{-5}

^aSpatial resolution and wall-normal spacings are given in inches.

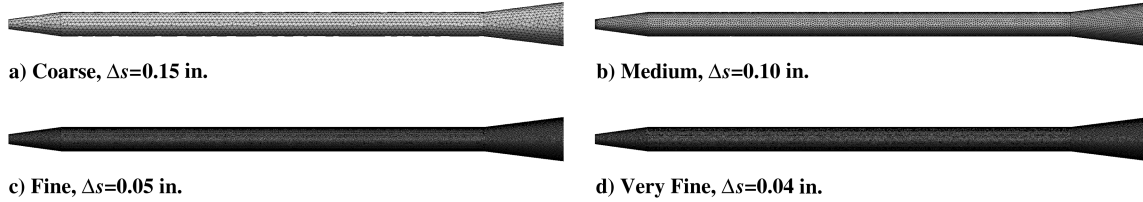


Fig. 6 Detailed view of the Pitot-static-probe-surface discretizations for the four levels of refinement.

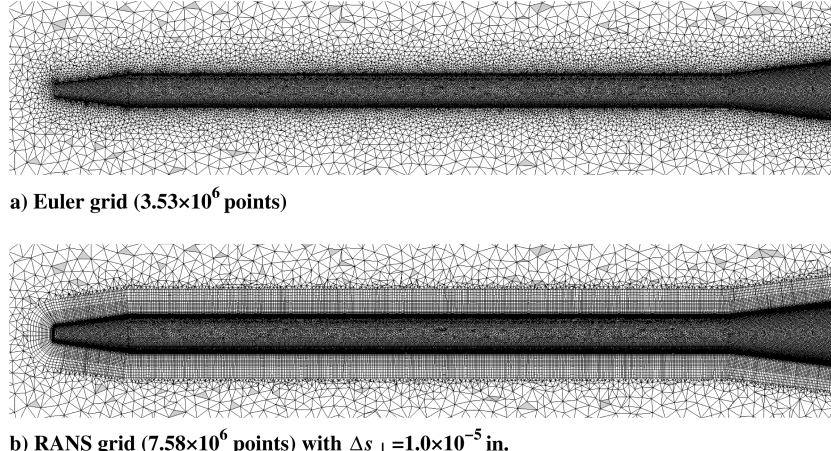


Fig. 7 Detailed view of the fluid-domain discretization grids comparing the Euler and RANS grids in the vicinity of the Pitot-static probe using the very fine surface-discretization element size of $\Delta s = 4.0 \times 10^{-2}$ in.

resolution on the entire aircraft. The far-field conditions of the computational domain specify M_∞ , altitude (p_∞ and ρ_∞), α , and β . The spatial scheme details include the least-squares formulation for gradients, Roe-type inviscid fluxes [24], finite-volume-based advection operator, and use of the van Albada limiter [25]. Solutions were obtained through implicit time integration using the backward Euler formulation.

In the presence of an adverse pressure gradient strong enough to cause flow separation, dramatic differences between Euler and Navier-Stokes solutions can be observed. However, if flow around the boom remains attached, it is reasonable to assume little difference between the pressure distribution at the edge of the viscous boundary layer and on the wetted surface of the probe. In transonic conditions, the simulated shock-wave location is affected by the boundary conditions, that is, Euler simulations typically predict shock waves at further aft locations than experiments [26–28] or Navier-Stokes simulations on the upper surface of thin wings. This discrepancy is assumed not to be a source of error for a simulated noseboom-mounted Pitot-static probe where shock waves are located near the convex/concave ramps and collars of the test-boom and probe geometries. Nevertheless, viscous simulations were performed to assess this assumption and quantify any differences.

Because of the separation of length scale and timescale between the aircraft and the static-pressure-port orifices, it was not feasible to compute the internal flow features of a Pitot-static probe attached to a noseboom on a full-scale fighter for any reasonably sized flight envelope within the timeframe required to support flight test. Furthermore, the total pressure port on the tip of the Pitot-static probe was not modeled, therefore any spillage effects were neglected.

The commercial grid-generation software ANSYS® ICEM CFD™ [29] was used to generate all the grids used in this work. The far-field domain was placed at 2.0×10^4 in. away from the center of the full T-38C aircraft with the largest tetrahedral elements restricted to having average edge lengths on the order of the aircraft mean chord. Based on the amount of resolution on the noseboom and Pitot-static probe, the number of grid points ranges from $(2.45 - 3.53) \times 10^6$. Figure 5 presents a side view of the full-aircraft

grid and a detailed view in the vicinity of the noseboom. For inviscid Euler simulations, tetrahedral elements fill the fluid domain with higher grid densities dedicated to the region of the boom and probe using a Delaunay-based (TGrid in ICEM CFD) grid-generation technique. Prism layers are then grown from the triangulated surface into the inviscid tetrahedron filled fluid domain for viscous simulations.

A. Analysis Methodology

Steady-state simulations were run until the global relative residual (based on continuity, momentum, and energy equations) reached a specified tolerance of 10^{-6} . The static-pressure error on the entire aircraft can then be visualized and specific points of interest can be extracted for comparison with the locations of the static-pressure ports present on the test T-38C. The distribution of static-pressure error is much more sensitive to surface-discretization irregularities than global aerodynamic loads like lift and drag due to its local nature and relatively small tolerances (less than 5%). When comparing to data from the flight test, the static-pressure-error correction, $\Delta p_{pc}/q_c = (p_\infty - p_{\text{measured}})/(p_{\text{total}} - p_\infty)$, (i.e., the quantity added to the measured pressure to obtain the true pressure) is used. The

Table 2 Static-pressure-error-correction CFD results for the straight probe using four levels of grid refinement using the straight Pitot-static probe

M_∞	α , deg	Static-pressure-error correction, $\Delta p_{pc}/q_c$				
		Coarse	Medium	Fine	Very fine	RANS
0.30	7.5	-0.073	-0.034	-0.028	-0.024	-0.029
0.40	5.0	-0.056	-0.031	-0.028	-0.027	-0.028
0.85	2.0	-0.041	-0.030	-0.029	-0.030	-0.030
0.90	1.0	-0.042	-0.031	-0.030	-0.033	-0.031
0.95	1.0	-0.042	-0.033	-0.033	-0.034	-0.034
1.05	1.0	-0.011	-0.001	0.001	0.000	0.000

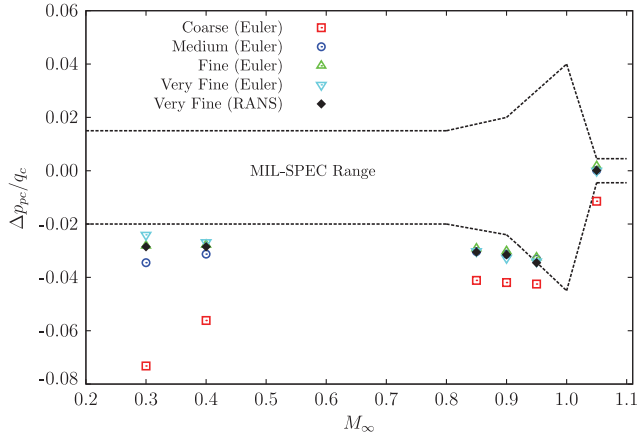


Fig. 8 Comparison of the static-pressure-error correction, $\Delta p_{pc}/q_c$, values for using four levels of grid refinement for the straight Pitot-static probe plotted against freestream Mach number M_∞ .

static-pressure-error correction is equal in magnitude and opposite of sign than the measured static-pressure error, $\Delta p/q_c$, from the CFD predictions.

B. Grid-Convergence Study

It is well known that grid topology, size, and quality can be nonnegligible sources of error in CFD results. A poor discretization can reduce a solution aimed to be globally second-order accurate to be zero-order accurate in the vicinity of poor elements. Structured-

grid approaches have the advantage of controlling the topology of the grid in nearly every location of interest at the expense of long lead times. Unstructured-grid approaches offer increased flexibility for complicated geometry and shorter lead times at the risk of a poor-quality (misaligned elements) discretization. In this work, a grid-convergence study was performed to identify errors due to a lack of spatial resolution or poorly constructed topologies. The four levels of spatial resolution used are provided in Table 1. Grid-resolution increases were confined to the region in the vicinity of the test boom and Pitot-static probe in an effort to dedicate computational resources to the location of interest. The levels of spatial refinement are visualized in Fig. 6, in which the resolution is refined by a factor of 3.75 from the coarse to very fine grids. A RANS grid was also generated using the very fine inviscid mesh as a starting point with 40 prism layers, as seen in Fig. 7. For this study, 0.1-in.-tall prisms were initially grown and then split to satisfy wall-normal-spacing requirements. The total height of the prism layers on the Pitot-static probe is 0.5 in. with a growth factor of 1.2 [30] and a first wall-normal spacing of $\Delta s_\perp = 1 \times 10^{-5}$ in. for a $y^+ \approx 1$ based on a probe-diameter Reynolds number of 10^6 . The probe Reynolds-number value is representative of typical aircraft flight conditions, in which Reynolds numbers based on mean chord are $\mathcal{O}(10^7)$.

Six flight-test conditions (given in Table 2) were simulated: two at low-altitude subsonic conditions and four at high-altitude transonic ($0.8 < M_\infty < 1.2$) conditions. The α values chosen are typical of steady-level flight of the T-38C at the Mach numbers listed. Each inviscid Euler simulation consumed between 1000 and 3000 core hours (8–24 h on 128 2.53 GHz Intel® Xeon® CPU cores), depending on the grid resolution used, whereas each viscous simulation consumed approximately 12,000 core hours (24 h on 512 2.53 GHz Intel® Xeon® CPU cores). The total computational

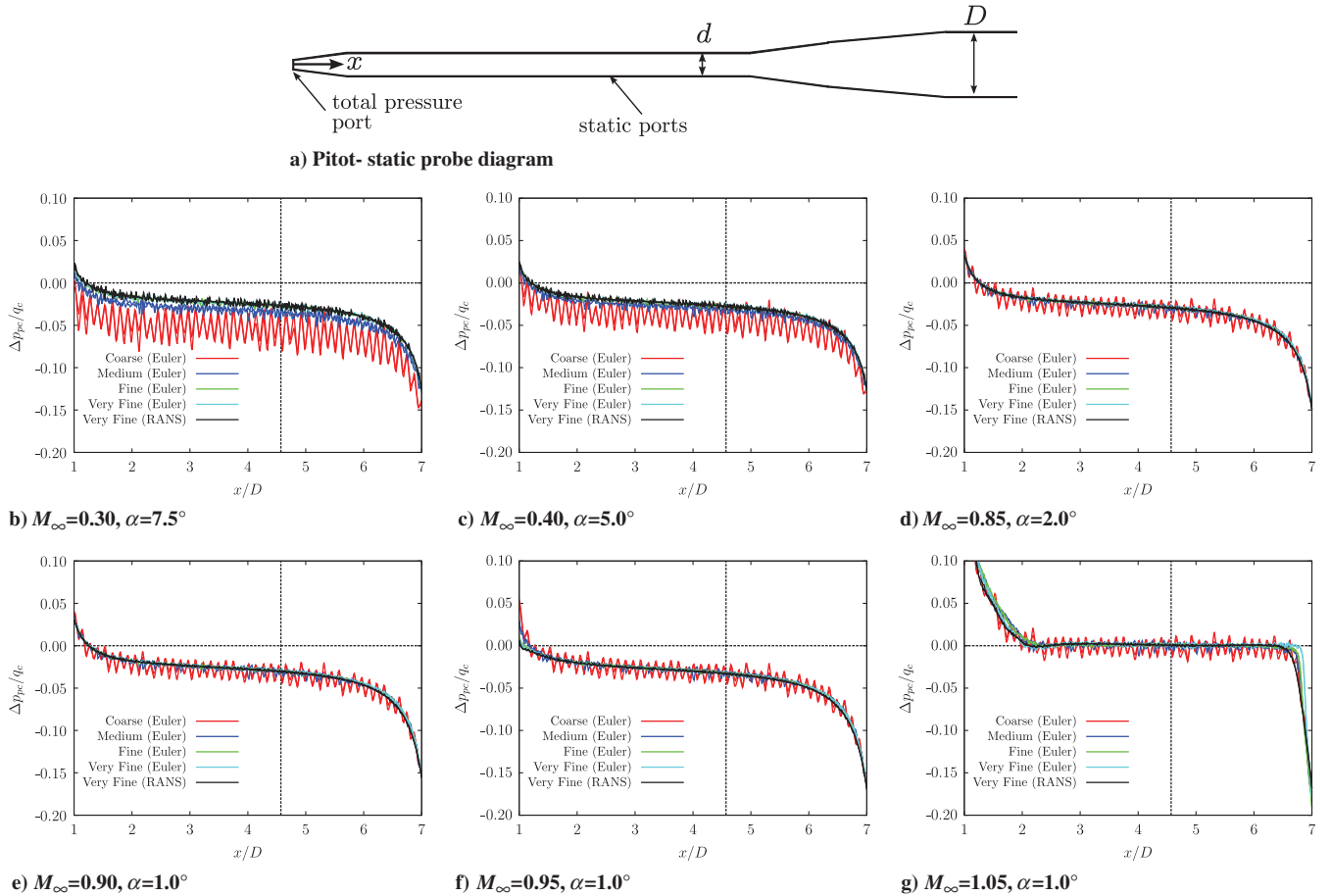


Fig. 9 Static-pressure-error correction, $\Delta p_{pc}/q_c$, is plotted against distance from the probe tip, x/D , for the four levels of grids used at a circumferential location of 36 deg from the bottom of the probe.

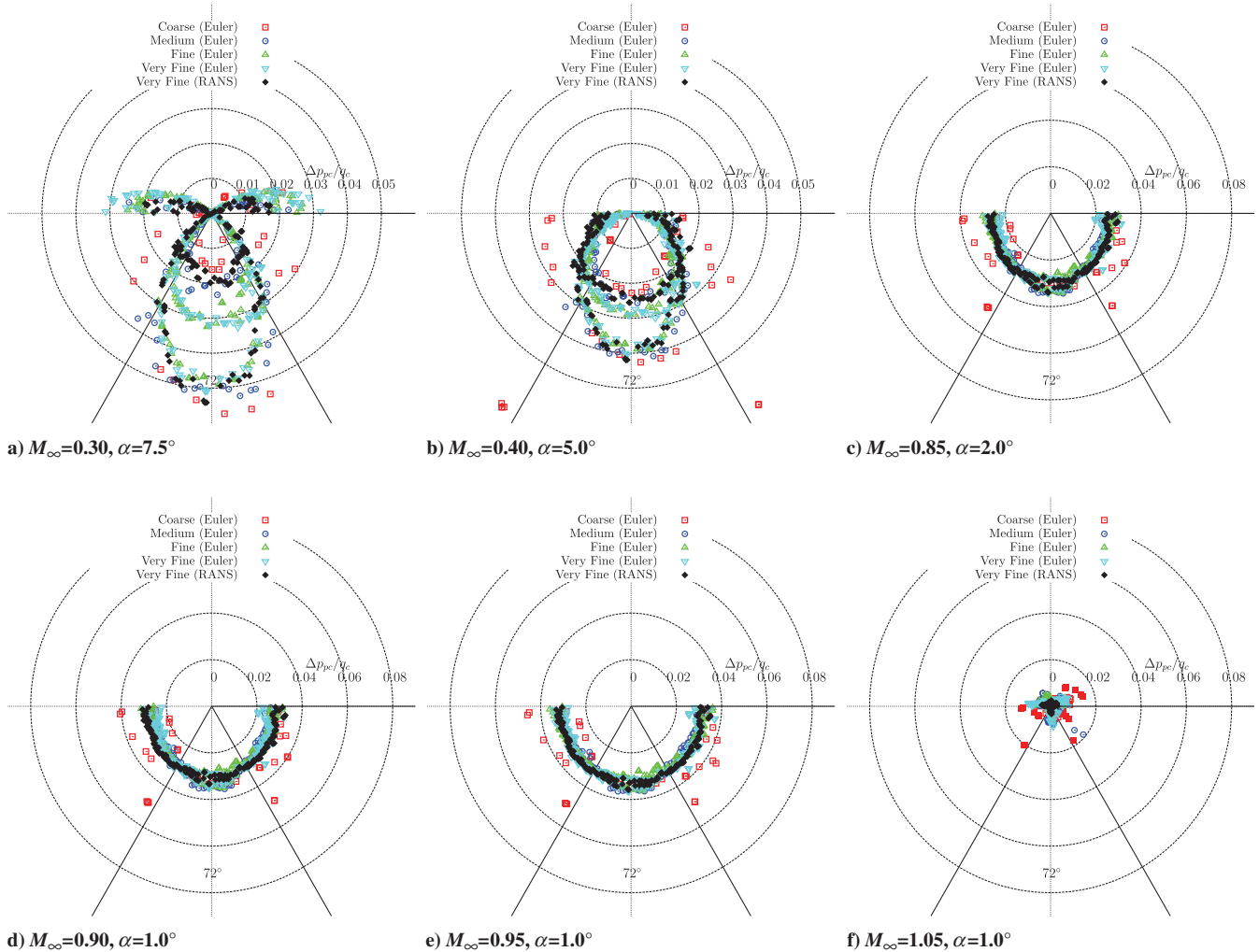


Fig. 10 Static-pressure-error correction, $\Delta p_{pc}/q_c$, is plotted against circumferential angle at $x/D \approx 4.6$ for the four levels of grids used.

expense for all the simulation results presented herein is approximately 160,000 core hours.

At low Mach numbers, the CFD predictions for the two finest grids are similar and significantly different from the coarsest grid, as seen in Table 2 and visualized in Fig. 8. The corrections predicted are outside of the MIL-SPEC range [1], which is shown in Fig. 8 as the area enclosed by the dashed lines. At transonic Mach numbers (0.85–0.95), the CFD predictions for the medium, fine, and very fine grids are very similar ($\Delta p_{pc}/q_c \approx -0.03$). At supersonic conditions, as the shock wave passes over the static-pressure-port locations, the error correction needed is reduced to a fraction of a percent for the medium, fine, and very fine grids.

The difference between the inviscid (Euler) and viscous (RANS) simulations is most prevalent at the slowest, highest α condition ($M_\infty = 0.3$). At this condition, the viscous methodology more accurately captures the adverse pressure gradient generated in the streamwise direction due to the curvature of the probe. This effect is nearly diminished at low α conditions, in which the streamwise and axial coordinates differ only by a single degree.

Figure 9 presents $\Delta p_{pc}/q_c$ CFD results against fuselage-station location (x/D) from the nose tip at constant circumferential locations of 36 deg. The predicted static-pressure-error-correction value is obtained where the lines of $\Delta p_{pc}/q_c$ intersect the vertical dashed line at $x/D \approx 0.46$; this is where the static ports are located on the T-38C test aircraft probe. Here, D is the largest diameter of the YAPS system, and x is the distance from the probe tip, as seen in Fig. 9a. In Fig. 9, it is clear that coarse-grid-resolution simulations reveal nonphysical oscillations that are on the order of magnitude of the errors of interest. The finest two grids yield nearly identical results

and demonstrate that grid independence was achieved. For the probe-surface mesh, consistent six-triangle nodes are desired, but impurities will exist due to the automatic grid-generation process. When the triangulation switches patterns, a local (nonphysical) spike in the static-pressure error can be observed, but global-force calculations (e.g., lift, drag) are not significantly influenced by these effects. Possible solutions to these grid-induced errors include grid refinement [31] or employing an anisotropic grid topology [32]; this section focuses on the former as a solution.

The radial distributions of $\Delta p_{pc}/q_c$ at the fuselage station where the static ports are located ($x/D \approx 4.6$) are presented in Fig. 10. Viscous effects are not a noticeable discriminant in the streamwise distribution, but are slightly more revealing when $\Delta p_{pc}/q_c$ is plotted against the circumferential location. These results demonstrate grid convergence, but also emphasize the importance of radial port placement at subsonic conditions, and the small error magnitude observed at supersonic conditions. Prior flight-test results [4] indicate that the error is a strong function of orifice circumferential position at high α conditions; this trend is also predicted by simulations as a slight disagreement between the inviscid and viscous results in Figs. 10a and 10b.

Figure 11 illustrates the regions of positive and negative errors from subsonic and supersonic freestream Mach numbers. Increased values of $\Delta p/q_c$ are typical in regions of decelerated flow, which is caused by forward-propagating pressure waves or adverse pressure gradients generated from the probe and test-boom ramps in subsonic flow. In the supersonic regime, $\Delta p/q_c$ regions are much more distinct, and the influence of the ramp is confined to an area nearer the ramp because pressure waves cannot travel upstream. In Fig. 11a

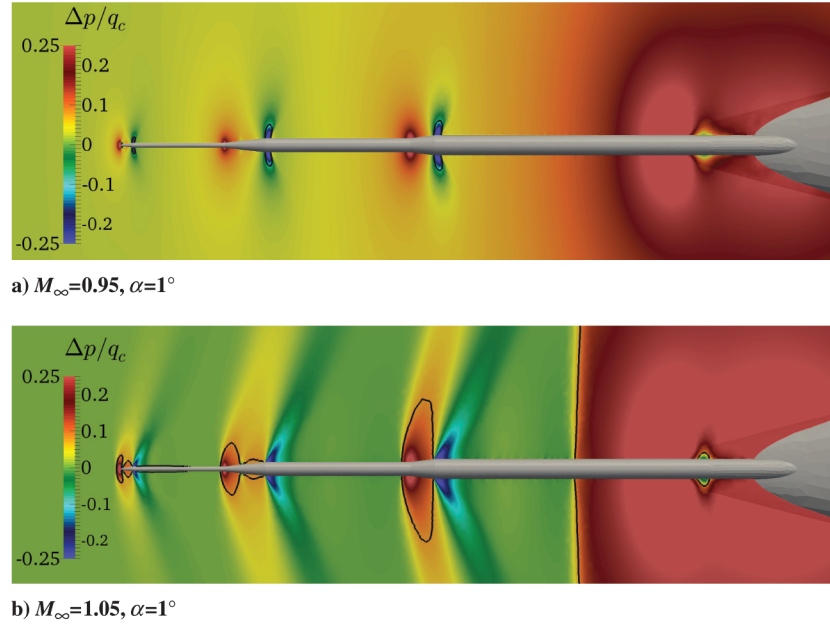


Fig. 11 Colored contours of $\Delta p/q_c$ overlaid with sonic lines and shock-wave locations.

small supersonic regions are located aft of the convex corners as the flow is accelerated, along with forward-propagating positive $\Delta p/q_c$ regions in front of the ramp/collars whereas in Fig. 11b the subsonic regions are located at the ramp/collar locations with zero error regions in front of each weak shock on the noseboom. These weak shock waves are accompanied by a clearly visible strong aircraft nose-cone bow shock wave.

V. Comparison with Flight Test

Simulation results using the very fine spatial-resolution grids are given in Table 3 and Fig. 12, along with the results from the USAF TPS flight tests [12]. The results from the CFD simulations agree well for the subsonic cases, but underestimate the correction needed in the transonic regime by approximately 0.5% for $M_\infty = 0.85$, and up to 1.5% for $M_\infty = 0.95$. However, for the supersonic case, the results are in good agreement with the flight test. The trend of increasing pressure correction with increasing Mach number is also captured well. These errors may be considered small for other CFD validation studies, but for this particular application, a few percent error in static pressure can amount to hundreds of feet of indicated altitude, depending on the flight speed and altitude. As mentioned previously, these discrepancies can limit the aircraft envelope in national airspace due to TPS, MIL-SPEC [1], and federal regulations [2,13].

The straight Pitot-static-probe geometry used in the initial simulations and in the flight test yielded static-pressure-correction values that were outside of the MIL-SPEC range for all subsonic cases. Historical data suggest that placing the static ports too near

the probe collar/ramp can induce errors at transonic flight conditions [33]. Pressure measurements at all distances from the collar/ramp will include some amount of error; only by analyzing the pressure distribution on the surface can a more resilient location be suggested. For the straight probe, the correction is nearest to meeting the MIL-SPEC of $\Delta p_{pc}/q_c = -0.02$ at a distance of approximately $2.25D$ aft of the probe tip. However, the x/D location where minimum static-pressure-error correction occurs is different for each M_∞ - α combination. As expected, the error-correction magnitude is larger for high subsonic Mach numbers. The tip of the probe influences the error correction needed further downstream for the supersonic case.

The effectiveness of two potential modifications that can reduce the needed correction in the transonic regime was also evaluated against the straight-probe flight-test results. The first is a larger-diameter probe chosen, so that the D/d ratio is closer to the values of 1.3–1.8 observed in previous studies [4,6], and smaller than the $D/d \approx 2.5$ of the flight-tested straight-probe design. The second is a compensating surface to offset the correction needed due to the influence of the test-boom ramp and aircraft nose cone. The surface grids of the two potential probes are shown in Fig. 13, and were simulated using the finest grid resolution of $\Delta s = 4.0 \times 10^{-2}$ in. Table 3 and Fig. 12 also include the results demonstrating the effectiveness of these two proposed design modifications. The larger-diameter design essentially predicts a constant offset for the error correction needed, yielding results modestly nearer to the MIL-SPEC range. The aerodynamically compensated probe predicts results that are roughly an order of magnitude smaller in the transonic regime, but the risk of overcompensation for the lowest

Table 3 Static-pressure-error-correction values given for the large-diameter and compensated probes (CFD), and for the straight probe (CFD and flight test)

M_∞	α , deg	Static-pressure-error correction, $\Delta p_{pc}/q_c$			
		Large diameter (Euler)	Compensated (Euler)	Straight (Euler/RANS)	Straight (flight test)
0.30	7.5	-0.016	0.014	-0.024 / -0.029	-0.026
0.40	5.0	-0.020	0.004	-0.027 / -0.028	-0.028
0.85	2.0	-0.023	0.000	-0.030 / -0.030	-0.036
0.90	1.0	-0.024	-0.001	-0.033 / -0.031	-0.038
0.95	1.0	-0.028	-0.006	-0.034 / -0.034	-0.050
1.05	1.0	0.003	-0.001	0.000 / -0.000	0.000

M_∞ case is a possible concern. Based on the agreement of the straight-probe flight test and the CFD results, there is confidence in the CFD predictions that a compensating probe could reduce the

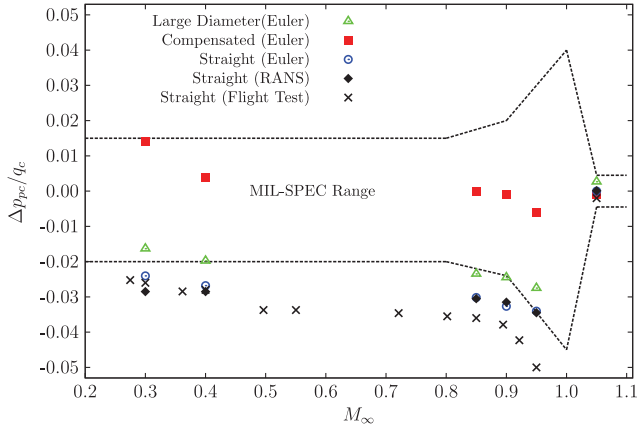


Fig. 12 Comparison of the static-pressure-error correction, $\Delta p_{pc}/q_c$, for the straight Pitot-static probe flight-test results (from formation and level acceleration/deceleration), and straight, large-diameter, and compensated-probe design CFD results plotted against freestream Mach number M_∞ .

error correction to more acceptable levels at typical operating Mach numbers.

The theoretical compensated probe was designed based on the suggestions of Werner and DeLeo [9] and DeLeo and Hagen [34]. The peak diameter ($\approx 0.46D$) is located aft of the static-port location of the straight test probe ($4.85D$ from the tip). The flow accelerates due to the favorable pressure gradient generated by the compensating surface. This surface reduces pressure at the upstream static port to a value near the freestream pressure p_∞ . The static port should be placed immediately upstream of the compensating surface to obtain the lowest possible error value. The ideal location to place a static-pressure port is where the error-correction line crosses zero for all Mach numbers; that point is located at approximately $4.6D$ from the boom tip for this particular setup, as indicated in Fig. 14. The compensated design has a very different error-correction profile than the straight probe that illustrates the need to properly place the static port. An approximately $3.5D$ long portion of the probe forward of the compensating surface reveals an error correction near the lower limit of the MIL-SPEC ($\Delta p_{pc}/q_c = -0.02$) for the high subsonic Mach numbers simulated. This compensated-probe design is capable of providing measurements that require little or no correction from an air-data computer. Figure 15 illustrates the circumferential dependence on $\Delta p_{pc}/q_c$ and demonstrates the superiority of the compensated probe design in the transonic regime.

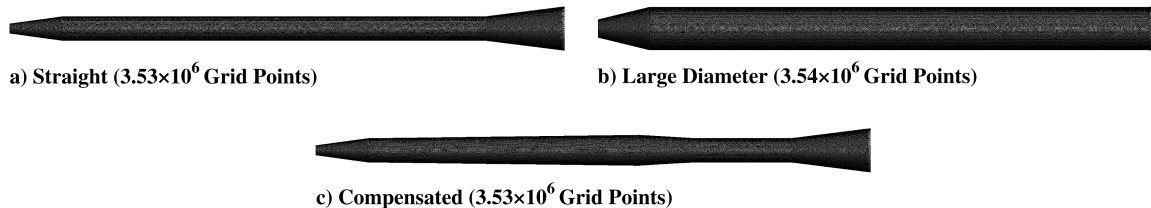


Fig. 13 Detailed view of the surface triangulations used for the large-diameter and aerodynamically compensated probes illustrating their geometric differences from that of the straight-probe geometry.

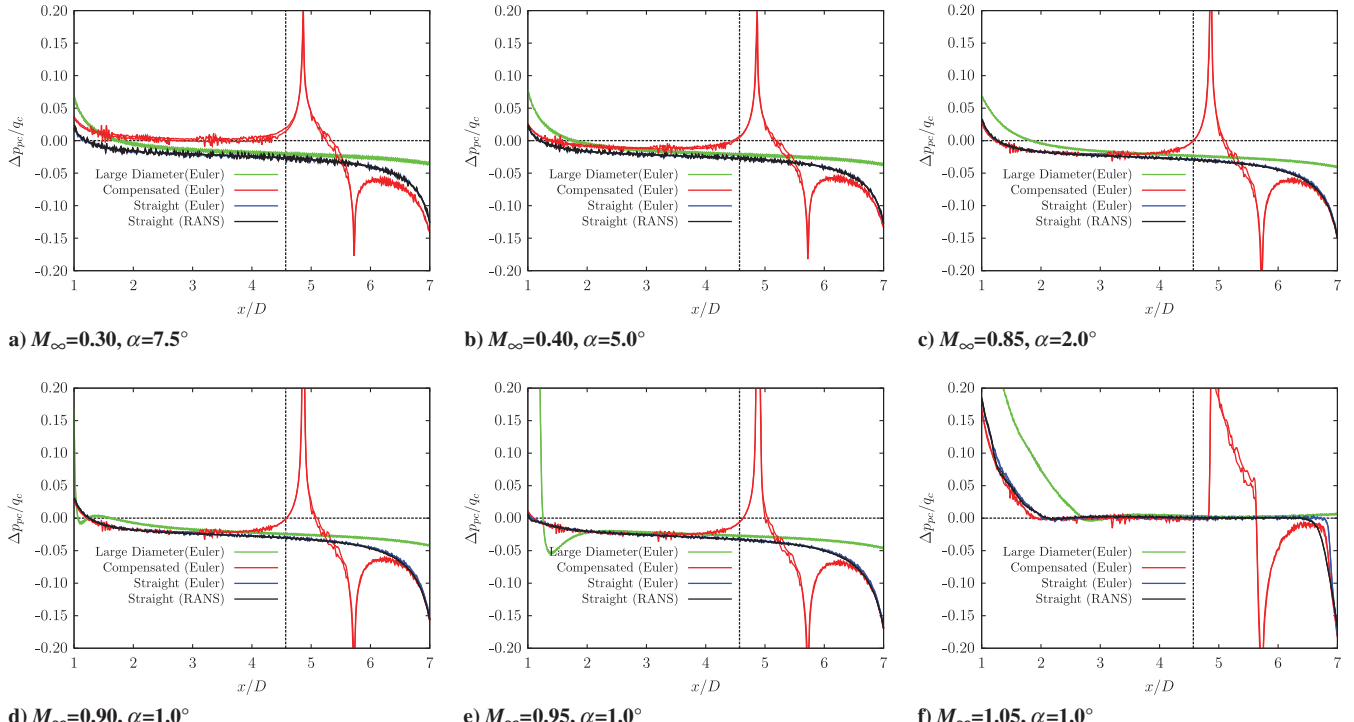


Fig. 14 Static-pressure-error correction, $\Delta p_{pc}/q_c$, is plotted against the fuselage station for the straight, large-diameter, and aerodynamically compensated designs at a circumferential location of 36 deg from the bottom of the probe.

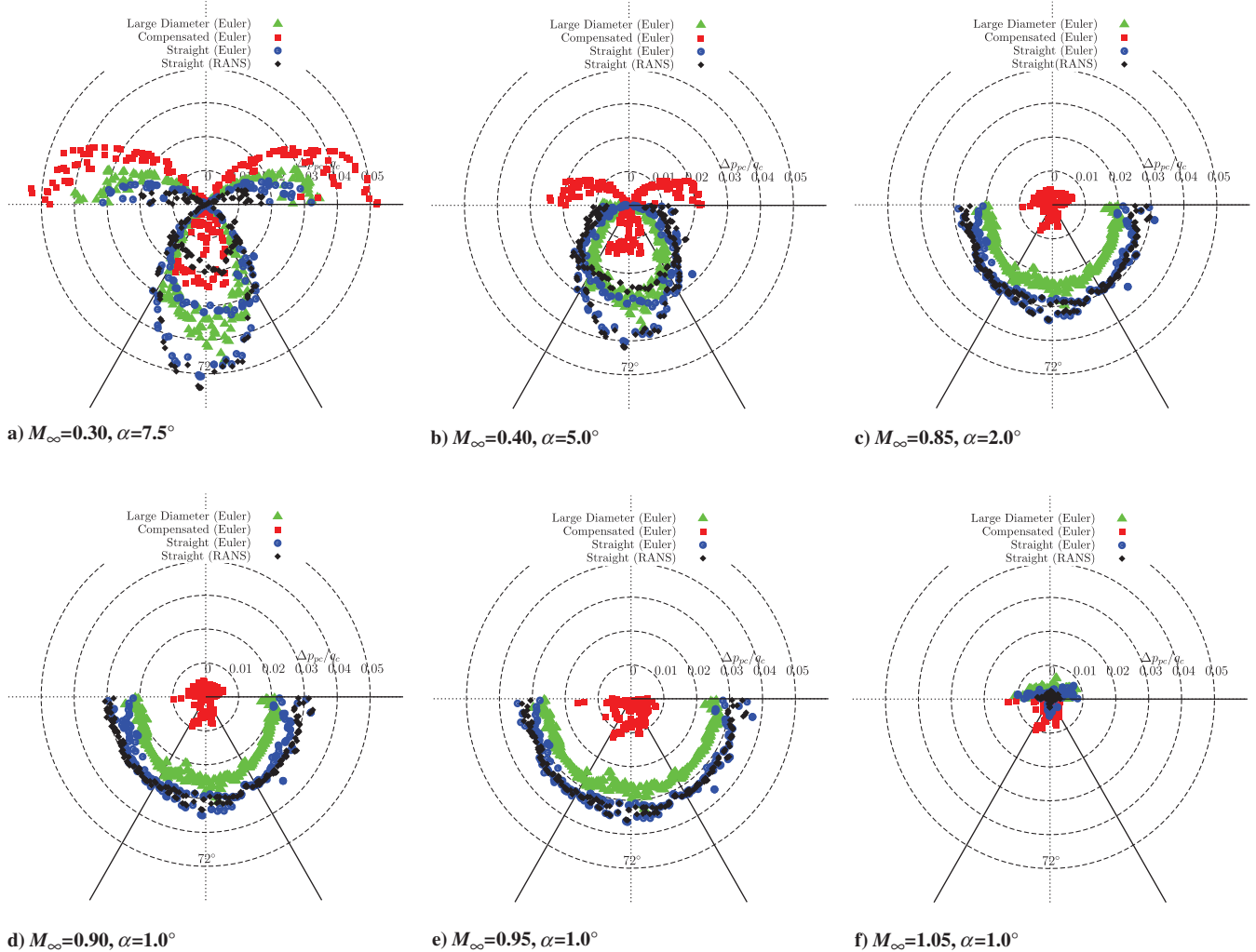


Fig. 15 Static-pressure-error correction, $\Delta p_{pc}/q_c$, is plotted against circumferential angle at $x/D \approx 4.6$ for the straight, large-diameter, and aerodynamically compensated designs.

VI. Conclusions

The findings presented herein focused on the CFD modeling considerations for estimating the static-pressure-error corrections needed for a test-noseboom-probe system mounted on a T-38C trainer aircraft used by the USAF TPS at Edwards Air Force Base, California. Current node-centered unstructured CFD methods utilizing a model of a realistic test-noseboom-probe system mounted to a T-38C aircraft, were able to predict results in relatively good agreement with flight-test data in the subsonic, transonic, and low supersonic regimes. The differences between inviscid (Euler) and viscous (RANS) predictions were observed to be negligible at low α conditions where the flow is attached. The findings also reveal that care must be taken when constructing the surface grid of the probe to ensure good cell quality and consistent surface triangulations to avoid nonphysical spikes in the surface pressure distribution in the vicinity of the static-pressure ports.

There is a vast amount of wind-tunnel and flight-test literature regarding Pitot-static-probe design and the important parameters that influence the amount of static-pressure error observed. The results presented herein highlight that CFD predictions were consistent with the trends seen in previous experimental/flight-test studies used to improve static-pressure error, including port location from ramp/collar, diameter ratio, and aerodynamic compensation. The placement of port locations and diameter ratio were shown to provide a lesser amount of error reduction than aerodynamic compensation. For aircraft that do not use air-data computers, the use of aerodynamic compensation is an elegant solution to reduce the static-pressure error observed by pilots in the cockpit and by autopilot

control systems. As demonstrated in the previous section, an aerodynamic compensating noseboom-probe system is a feasible solution to reduce the static-pressure error of the test-noseboom Pitot-static system installed on the high-performance USAF TPS T-38C trainer fleet.

Acknowledgments

The authors would like to acknowledge the guidance and support of the U.S. Air Force Test Center, specifically the 412th Test Wing Test Engineering Group and the U.S. Air Force Test Pilot School.

References

- [1] "Installation and Inspection of Pitot-Static Pressure Systems," U.S. Air Force MIL-P-26292C, Wright-Patterson AFB, 1969.
- [2] "Operations in Reduced Vertical Separation Minimum Airspace (RVSM)," Part 91, Appendix G, Sec. 2, <http://www.faa.gov/> [retrieved 15 July 2014].
- [3] Bhamidipati, K. K., Lechniak, J. A., and Woolf, R. K., "T-38C Noseboom Pressure and Velocity Study Using Computational Fluid Dynamics," U.S. Air Force Flight Test Center AFFTC-TIM-11-06, Edwards AFB, CA, 2012.
- [4] Gracey, W., "Measurement of Static Pressure on Aircraft," NACA Rept. 1364, 1956.
- [5] DeLeo, R. V., and Hagen, F. W., "Flight Calibration of Aircraft Static Pressure Systems," Federal Aviation Agency, Systems Research and Development Service Rept. RD-66-3, Rosemount Engineering Co. Rept. 76431, Minneapolis, MN, 1966.
- [6] Wuest, W., "Pressure and Flow Measurement," AGARD AG-160, Vol. 11, AGARD Flight Test Instrumentation Series, 1980.

- [7] Haering, E. A., "Airdata Measurement and Calibration," NASA TM-104316, 1995.
- [8] McKeon, S., "Static Pressure Correction in High Reynolds Number Fully Developed Turbulent Pipe Flow," *Measurement Science and Technology*, Vol. 13, No. 10, 2002, pp. 1608–1614. doi:10.1088/0957-0233/13/10/314
- [9] Werner, F. D., and DeLeo, R. V., "Static Pressure Probe," Rosemount Engineering Co., Minneapolis, MN, U.S. Patent 3,120,123, filed 8 Nov. 1960, issued 4 Feb. 1964.
- [10] Luo, S., and Bao, Y., "Computation of Transonic Aerodynamically Compensating Pitot Tube," *Journal of Aircraft*, Vol. 25, No. 6, 1988, pp. 544–547. doi:10.2514/3.45620
- [11] Latif, A., Masud, J., Sheikh, S. R., and Pervez, K., "Robust Design of an Aerodynamic Compensation Pitot-Static Tube for Supersonic Aircraft," *Journal of Aircraft*, Vol. 44, No. 1, 2007, pp. 163–169. doi:10.2514/1.22775
- [12] Woolf, R. K., "Analysis of T-38C Flight Test Noseboom Static Source Error Corrections," U.S. Air Force 773rd Flight Systems Integration Squadron Internal Office Memo, Edwards AFB, CA, 2013.
- [13] "Code of Federal Regulations (EFCR)," Part 23, Secs. 1323 and 1325; and Part 91, Sec. 217, <http://www.ecfr.gov> [retrieved 15 July 2014].
- [14] Koobus, B., and Farhat, C., "Second-Order Time-Accurate and Geometrically Conservative Implicit Schemes for Flow Computations on Unstructured Dynamic Meshes," *Computer Methods in Applied Mechanics and Engineering*, Vol. 170, Nos. 1–2, 1999, pp. 103–129. doi:10.1016/S0045-7825(98)00207-2
- [15] Koobus, B., and Farhat, C., "On the Implicit Time Integration of Semi-Discrete Viscous Fluxes on Unstructured Dynamic Meshes," *International Journal for Numerical Methods in Fluids*, Vol. 29, No. 8, 1999, pp. 975–996. doi:10.1002/(ISSN)1097-0363
- [16] Farhat, C., Geuzaine, P., and Grandmont, C., "The Discrete Geometric Conservation Law and the Nonlinear Stability of ALE Schemes for the Solution of Flow Problems on Moving Grids," *Journal of Computational Physics*, Vol. 174, No. 2, 2001, pp. 669–694. doi:10.1006/jcph.2001.6932
- [17] Geuzaine, P., Grandmont, C., and Farhat, C., "Design and Analysis of ALE Schemes with Provable Second-Order Time-Accuracy for Inviscid and Viscous Flow Simulations," *Journal of Computational Physics*, Vol. 191, No. 1, 2003, pp. 206–227. doi:10.1016/S0021-9991(03)00311-5
- [18] CMSoft, Inc., "The AERO Suite of Codes," Ver. 1.1, CMSoft, Palo Alto, CA, <http://www.cmsoftinc.com> [retrieved 12 Oct. 2012].
- [19] Geuzaine, P., Brown, G., Harris, C., and Farhat, C., "Aeroelastic Dynamics Analysis of a Full F-16 Configuration for Various Flight Conditions," *AIAA Journal*, Vol. 41, No. 3, 2003, pp. 363–371. doi:10.2514/2.1975
- [20] Lechniak, J. A., and Bhamidipati, K. K., "Fluid–Structure Interaction Evaluation of F-16 Limit Cycle Oscillations," AIAA Paper 2012-0042, Jan. 2012, pp. 1–9.
- [21] Lechniak, J. A., Bhamidipati, K. K., and Pasiliao, C. L., "Characterizing the Aerodynamic Influence of F-16 Stores on Limit Cycle Oscillations Using Aero-Structure Simulation," AIAA Paper 2012-3340, June 2012, pp. 1–13.
- [22] Reasor, D. A., Lechniak, J. A., Bhamidiapti, K. K., Besson, M. R., and Pasiliao, C. L., "Fluid–Structure Modeling and Simulation of a Modified KC-135R Icing Tanker Boom," AIAA Paper 2013-0053, Jan. 2013, pp. 1–18.
- [23] Spalart, P. R., and Allmaras, S. R., "A One-Equation Turbulence Model for Aerodynamic Flows," AIAA Paper 1992-0439, Jan. 1992, pp. 1–22.
- [24] Roe, P. L., "Approximate Riemann Solvers, Parameter Vectors, and Difference Schemes," *Journal of Computational Physics*, Vol. 43, No. 2, 1981, pp. 357–372. doi:10.1016/0021-9991(81)90128-5
- [25] van Albada, G. D., van Leer, B., and Roberts, W., "A Comparative Study of Computational Methods in Cosmic Gas Dynamics," *Astronomy and Astrophysics*, Vol. 108, No. 1, 1982, pp. 76–84.
- [26] Magnus, R., and Yoshihara, H., "Inviscid Transonic Flow over Airfoils," *AIAA Journal*, Vol. 8, No. 12, 1970, pp. 2157–2162. doi:10.2514/3.6080
- [27] Schmidt, W., Jameson, A., and Whitfield, D., "Finite-Volume Solutions to the Euler Equations in Transonic Flow," *Journal of Aircraft*, Vol. 20, No. 2, 1983, pp. 127–133. doi:10.2514/3.56723
- [28] Sankar, L. N., Malone, J. B., and Schuster, D., "Euler Solutions for Transonic Flow Past a Fighter Wing," *Journal of Aircraft*, Vol. 24, No. 1, 1987, pp. 10–16. doi:10.2514/3.45404
- [29] ICEM CFD, Ver. 14.5, ANSYS, Canonsburg, PA, ANSYS, Inc., <http://www.ansys.com> [retrieved 26 Dec. 2013].
- [30] Nichols, R. H., "Turbulence Models and Their Application to Complex Flows," Technical Rept. Rev. 4.01, Univ. of Alabama at Birmingham, Birmingham, AL, 2010.
- [31] Ferziger, J., and Perić, M., *Computational Methods for Fluid Dynamics*, 3rd ed., Springer, Berlin, Germany, 2002, pp. 334–336.
- [32] Blazek, J., *Computational Fluid Dynamics: Principles and Applications*, 2nd ed., Elsevier, Oxford, 2005, pp. 395–397.
- [33] Lock, C. N. H., Knowler, A. E., and Pearcey, H. H., "The Effect of Compressibility on Static Heads," Aeronautical Research Council, Rept. and Memorandum No. 2386, 1943.
- [34] DeLeo, R. V., and Hagen, F. W., "Model 855: Aerodynamically Compensated Pitot-Static Tube," Rosemount Engineering Co., Minneapolis, MN, Bulletin 116010, Nov. 1963.